STEM Imaging with Beam-Induced Hole and Secondary Electron Currents

William A. Hubbard, Matthew Mecklenburg, Ho Leung Chan, and B. C. Regan

STEM imaging with beam-induced hole and secondary electron currents

William A. Hubbard,[1, 2] Matthew Mecklenburg,[3] Ho Leung Chan,[1, 2] and B. C. Regan[1, 2]

[1]*Department of Physics and Astronomy, University of California, Los Angeles, CA 90095, U.S.A.*

[2]*California NanoSystems Institute, University of California, Los Angeles, CA 90095, U.S.A.*

[3]*Core Center of Excellence in Nano Imaging, University of Southern California, Los Angeles, California, 90089, U.S.A.*

In standard electron beam-induced current (EBIC) imaging, the scanning electron beam creates electron-hole pairs that are separated by an in-sample electric field, producing a current in the sample. In standard scanning electron microscopy (SEM), the scanning electron beam ejects secondary electrons (SE) that are detected away from the sample. While a beam electron in a scanning transmission electron microscope (STEM) can produce many electron-hole pairs, the yield of SE is only a few percent for beam energies in the range 60–300 keV, making the latter signal much more difficult to detect on-sample as an EBIC. Here we show that the on-sample EBIC in a STEM registers both SE emission and capture as holes and electrons, respectively. Detecting both charge carriers produces differential image contrast not accessible with standard, off-sample SE imaging. In a double-EBIC imaging configuration incorporating two current amplifiers, both charge carriers can even be captured simultaneously. Compared to the currents produced in standard EBIC imaging, which only highlights the regions in a sample that contain electric fields, the EBIC produced by SE, or SEEBIC, are small (pA-scale). But SEEBIC imaging can produce contrast anywhere in a sample, exposing the texture of buried interfaces, connectivity, and other electronic properties of interest in nanoelectronic devices, even in metals and other structures without internal electric fields.

I. INTRODUCTION

Transmission electron microscopy (TEM) is a powerful, high-resolution technique that can be applied to study functioning nanoelectronic systems *in situ*. Conventional TEM excels at determining the physical structure of the sample, namely the position and identity of the sample's constituent atoms. While this (physical) structure dictates many of the sample's properties, in devices it frequently is only of secondary interest. A device's function is often determined by its electronic, optical [1], or thermal [2] structure, to which conventional TEM is not directly sensitive.

In electron beam-induced current (EBIC) imaging, a focused electron beam is scanned across a sample that is attached to a transimpedance amplifier (TIA). Associating the measured sample current with the beam position forms the EBIC image [3, 4]. EBIC imaging has been used extensively to map electric fields that are intrinsic to the sample, such as those in Si dislocation defects [5–7] and in solar cells [8–12], and related properties, such as carrier lifetimes, diffusion lengths, defect energy levels, and surface recombination velocities [4, 13]. In these experiments, a local electric field generates the EBIC by separating electron-hole pairs produced by the primary beam. Because one primary electron can create thousands of electron-hole pairs [14, 15], this process has gain and the resulting signals are relatively large. Most EBIC studies have been conducted in a scanning electron microscope (SEM) [4, 6]. EBIC imaging for the purpose of mapping electric fields has also been extended to scanning TEM (STEM), where TEM's better electron optics and electron-transparent samples both contribute to improved spatial resolution [11, 16–19].

Here we demonstrate that STEM EBIC is sensitive to secondary electron (SE) emission, a much smaller signal distinct from the conventional electric field- and beam absorption-related EBIC signals. SE are electrons ejected from the sample by interactions with the primary beam. We have generated images where the contrast is dominated by SE emission and capture. Employing a 'double EBIC' imaging configuration, where two neighboring electrodes are connected to separate TIAs, allows us to collect, separately, both some of the emitted SE and all of the holes left behind. Unlike conventional TEM, secondary electron emission EBIC (SEEBIC) — and especially STEM SEEBIC — is directly sensitive to electronic properties; it can be used to assess connectivity and conductivity, and shows promise for mapping work function. Much of STEM SEEBIC's revelatory strength derives from its ability to directly detect holes, which is impossible for an off-sample SE detector.

II. THEORY

We consider a region on the sample that, if insulating, might be scarcely larger than the probe size, but if conducting encompasses the full extent of the electrically connected area. When the microscope's electron beam is incident on this region, we approximate the steady-state current balance with [20, 21]:

$$I_B + I_{in} = I_T + I_A + I_{BS} + I_{SE} + V_S/R_S + I_{out} \quad (1)$$

where I_B is the incident primary beam current, I_T is the transmitted beam current, I_A is the absorbed beam current, I_{BS} is the backscattered current, I_{SE} is the secondary electron current, and V_S and R_S are the beam-induced sample potential (due to charging) and effective resistance to ground, respectively. The terms with lower-case subscripts, I_{in} and I_{out}, represent on-sample device

currents that can be controlled and/or measured, perhaps in the absence of the electron beam. In this paper we consider only bare electrodes where one end of the 'device' is floating, in which case $I_{in} = 0$.

Very generally, the secondary electron signal is easiest to detect in devices configured to be floating, or nearly so (i.e. with an effective device impedance $R \gtrsim 10$ MΩ, and preferably $\gg$ GΩ). Otherwise the SE current I_{SE} is obscured by the Johnson noise current $\delta I = \sqrt{4k_BTB/R}$, where k_BT is the thermal energy and B is the amplifier bandwidth. For this reason, one might also take SEE-BIC to stand for 'single-ended' EBIC. Standard electric-field-based EBIC, in contrast, requires a low-impedance connection to the side of the device opposite the TIA to prevent charging.

In TEM generally, and in the cases of interest here, the largest term on the right-hand side of Eq. 1 is $I_T \simeq I_B$, while I_A and I_{BS} are mostly negligible [20–22]. In SEM, where instead typically $I_T = 0$, the $I_A \simeq I_B$ is a large background that makes observing the smaller I_{SE} via EBIC difficult. In an electrically isolated area, SE emission leads to charging [20] and $I_{SE} = -V_S/R_S$. If instead there is a low-impedance path to ground, or a virtual ground consisting of the input to a TIA, little charging occurs and a current $I_{out} = -I_{SE}$ is generated. In other words, a positive hole current flows into the amplifier that is equal and opposite to the negative SE current leaving the sample. For the TIA case I_{out} provides the SEEBIC signal, which can be mapped pixel by pixel, as the beam scans, to produce an image (Fig. 1).

The SE current detected depends on four multiplicative factors [22, 23]. First, the rate of secondary generation is determined by the primary beam energy E_B, the beam current I_B, and properties of the irradiated material. Second, the fraction of these secondaries that make it to the sample surface is determined by their mean free path (MFP) and distance to the surface. Third, the work function Φ_W (or the electron affinity χ for insulators) and surface potential V_S determine the escape probability once at the surface. Finally, the fraction of the escaped electrons that are counted by the detector depends on the efficiency and geometry of the detection apparatus, including the local electric and magnetic fields.

While calculating any of these factors is usually nontrivial, the SEEBIC case described above, where the beam is incident on a conductor connected to the TIA (see Eq. 1), is an exception: the fourth factor is unity. In other words, the electrode struck by the beam functions as an SE detector with perfect detection efficiency (to within a sign). The net hole current (see [21] for a detailed discussion) is detected by the TIA, unlike the case for an off-sample SE detector, where some SE might hit the detector and some might not.

To account for the physics underpinning the first and third factors, we adopt the following approximate expres-
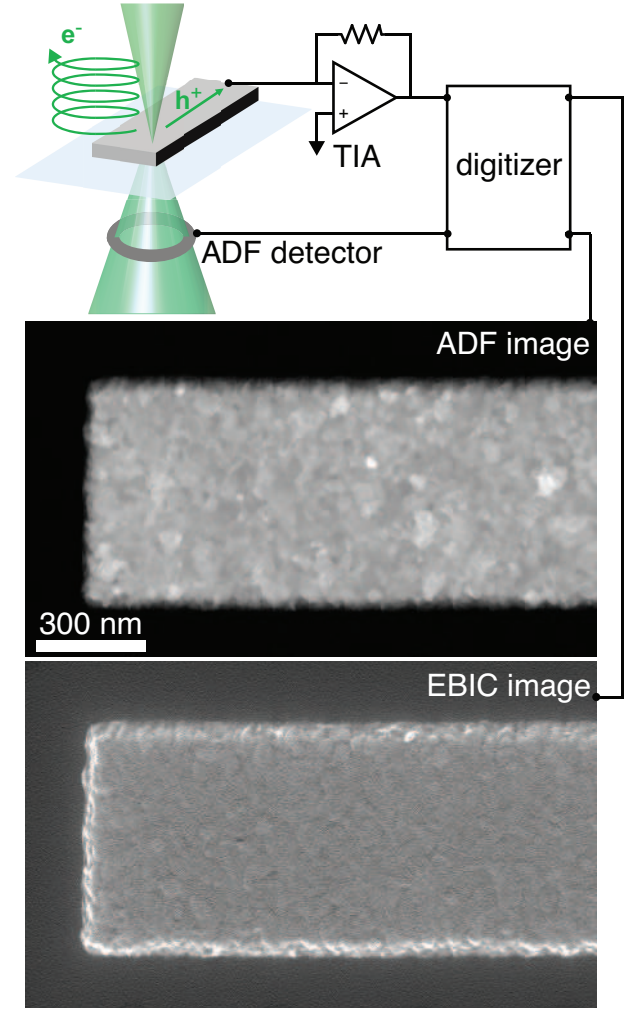

Figure 1. **STEM SEEBIC imaging of a metal electrode.** (*top*) A cartoon representation of the basic set-up shows the electron beam rastering over a bare Al electrode. Scattered electrons produce the usual annular dark-field (ADF) image (*middle*). SE ejected from the electrode leave holes behind, producing a positive current and corresponding bright contrast in the EBIC image (*bottom*). The imaged electrode is maintained at virtual ground by the transimpedance amplifier (TIA).

sion [15, 24] describing the scaling of I_{SE}:

$$I_{SE} \propto \frac{I_B}{E_B} \int_{eV_S}^{\infty} \frac{E_{SE}\, dE_{SE}}{(E_{SE} + \Phi_W)^4}$$
$$= \frac{I_B}{E_B} \times \frac{3eV_S + \Phi_W}{6(eV_S + \Phi_W)^3}, \text{ for } eV_S \geq 0. \quad (2)$$

Here E_{SE} is the SE energy relative to the vacuum zero level. Only electrons with $E_{SE} > 0$ can escape.

The integral given in Eq. 2 is most appropriate in the non-relativistic limit, and more careful analyses based on Bethe's relativistic stopping power relation [15, 25] or dielectric theory [25] give I_{SE} scaling that is weaker than

$1/E_B$. However, this simpler expression, commonly used to describe SE in SEM [15], is sufficient for our modest quantitative purposes.

In place of the usual integration limit of 50 eV, the conventional upper energy limit for secondary electrons [15], we use infinity in Eq. 2. This substitution simplifies the result and introduces only a small error ($\sim 3\%$). Note, however, that unity-detection-efficiency EBIC is fundamentally insensitive to backscattered electrons (where the charge originates in the primary beam, not the sample), and cannot distinguish between Auger electrons and SE. Furthermore, the number of high energy SE increases with increasing primary electron energy [26], and our STEM accelerating voltages are high (80–300 kV) compared to the usual SEM EBIC case. Thus this substitution also has several physical motivations.

Regarding the second of the four multiplicative factors mentioned above: the MFP for a SE in a material depends on the SE energy and the electron density of the material [24]. In general the SE MFP is shorter in materials with higher conductivity [24], with metals and insulators having SE MFPs of a few nanometers and 10's of nanometers, respectively [27, 28]. Because of the shortness of the MFPs, SEEBIC imaging tends to be more sensitive to the sample's surface, as opposed to its bulk, than conventional TEM imaging modes.

III. EXPERIMENTAL DETAILS

Silicon wafers 200 μm-thick and coated with 800 nm of SiO_2 and 20 nm of Si_3N_4 were selectively etched with KOH to reveal SiO_2/Si_3N_4 membranes on which Ti/Pt (5/25 nm) electrodes were patterned optically. (This 'slash' notation lists materials in the order in which they are deposited, here indicating a 5 nm titanium adhesion layer covered with 25 nm of platinum.) Additional features were patterned on these substrates via electron beam lithography, and then the supporting oxide was removed with an HF vapor etch (leaving the nitride) to make the samples electron-transparent. Unless otherwise noted, all imaging took place in an FEI Titan 80-300 S/TEM with an 80 kV accelerating voltage and a beam current of $\sim$30 pA, as measured with a Faraday cup [21]. A TIA (FEMTO DLPCA-200), connected to the sample via a biasing holder (Hummingbird Scientific), converted the EBIC into a voltage signal that was digitized along with the STEM detector signals [18]. In some cases, two TIAs connected to two different electrodes on the sample were used to simultaneously generate two EBIC images ('double EBIC'). The EBIC scans presented here are 256×256 pixels, and were acquired with a dwell time of $\sim$2.5 ms at each pixel (3 minutes per frame). No filtering (e.g., for 60 Hz noise) has been applied to any of the images.
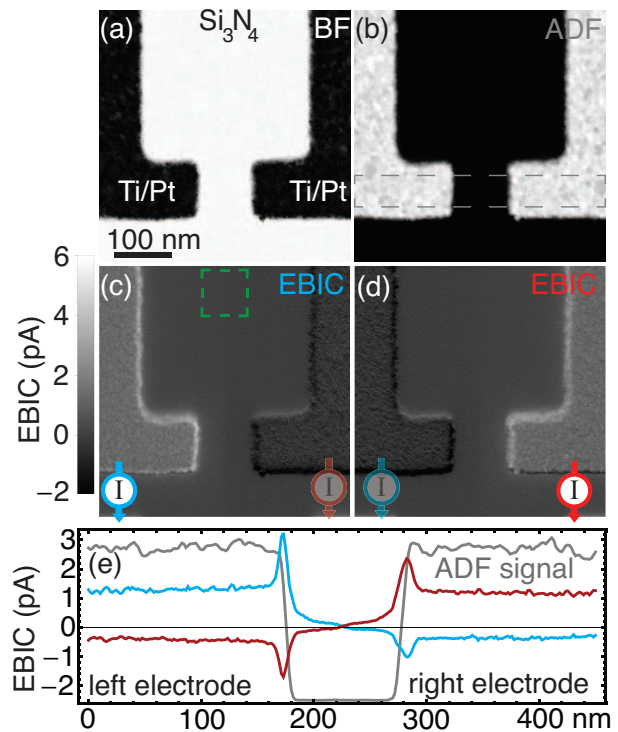
Figure 2. **Conventional STEM, and double STEM SEEBIC imaging of Ti/Pt electrodes.** The simultaneously-acquired (a) bright field (BF), (b) annular dark field (ADF), and (c,d) STEM EBIC images show Ti/Pt (5/25 nm) electrodes on a Si_3N_4 membrane. TIAs are connected to the electrodes as indicated by the blue and red symbols in the STEM EBIC images, with the symbol shown as opaque in the image generated by that TIA. Bright/dark contrast corresponds to positive/negative current, as indicated by the legend for (c,d) to the left of (c). The gray, blue, and red plots in (e) show line profiles from (b), (c), and (d) taken in the region indicated by the gray rectangle in (b). The gray plot is in arbitrary units and the blue and red plots use the scale on the y-axis. The images (a–d) have been rotated 90° counter-clockwise, so that the fast scan direction is bottom-to-top. EBIC values in (c,d) are given relative to their respective averages from the region outlined in green in (c).

IV. RESULTS AND DISCUSSION

We first illustrate the basics of SEEBIC imaging with a simple example, showing images of a single bare 100 nm-thick aluminum electrode on a 15/15 nm Si_3N_4/Al_2O_3 membrane (Fig. 1). As indicated in the Fig. 1 cartoon (*top*), as the focused electron beam rasters over the sample, several signals are digitized in parallel: the signals from the usual STEM detectors, and the EBIC signal. Here just the annular dark field (ADF) is shown (*middle*) together with the EBIC image (*bottom*). The EBIC image shows contrast that is unlike, e.g., that of the ADF image, and is very similar to that of an SE image acquired in an SEM [21], which already points to SE as the source of the contrast. For instance, the electrode edges

appear markedly brighter in the EBIC image (and not in the ADF image), exhibiting the enhanced emission that gives the well-known edge contrast of SE imaging [15].

To further implicate SE, we employ 'double EBIC' imaging, connecting separate TIAs to two separated, bare electrodes on a Si_3N_4 membrane (Fig. 2). In each of the conventional STEM images, the two 5/25 nm Ti/Pt electrodes give identical contrast: primarily dark in the BF detector (Fig. 2a), and primarily bright in the ADF detector (Fig. 2b), with small variations due to different grain orientations in the polycrystalline metal. In the two STEM EBIC images (Fig. 2 c,d), however, the electrode contrast flips depending upon whether the TIA generating the image is connected to the electrode being imaged, or not.

This contrast reversal is expected for SEEBIC. SE emitted from an electrode connected directly to the TIA generate positive current via the holes that are left behind. SE emitted from elsewhere in the sample, e.g., the opposing electrode, can also be captured by the electrode connected to the TIA, and generate a corresponding negative current [21]. (Replacing, for instance, the red TIA connected to the right electrode in Fig. 2 with a ground connection would mean that Fig. 2d was not acquired, but Fig. 2c would be unchanged.) As explained earlier, the connected electrode functions as an SE emission detector with unit efficiency. Since the beam-electrode interaction physics is independent of the electrode-TIA connections, with two amplifiers (or two sequential measurements on different electrodes) we can calibrate the efficiency of SE capture precisely. Here the direct electrode captures a surprisingly [21] large 20–50%, depending upon the emission location, of the SE emitted from the opposing electrode (Fig. 2e). As seen in the EBIC images (Figs. 2c–d) and the line profiles (Fig. 2e), both the efficiency of SE generation and emission, and the efficiency of SE capture, are evidently enhanced at the electrode edges (again exhibiting the expected SE edge contrast effect), while these efficiencies are comparatively uniform within an electrode. Note that, were double EBIC imaging to be employed in standard, electric-field-based EBIC, the electron and hole currents would have identical magnitudes [21]. Thus, having an electron current that is smaller than the hole current also supports the SE hypothesis.

The EBIC signals from the membrane show a subtle but unmistakable step at the midpoint between the electrodes, visible (all the way from top to bottom) in the images (Fig. 2c-d) and the plot (Fig. 2e). This step indicates that the membrane has some conductivity: a hole created by SE emission is attracted to its image charge (there are no intrinsic or externally applied electric fields) and heads to the nearest electrode (or, more precisely, takes the least resistive path toward ground), regardless of whether the inter-electrode gap is small or not. With an off-sample SE detector [23], such differential contrast is unavailable; both electrodes give the same contrast (as in the BF and ADF images), and there is no dividing line.
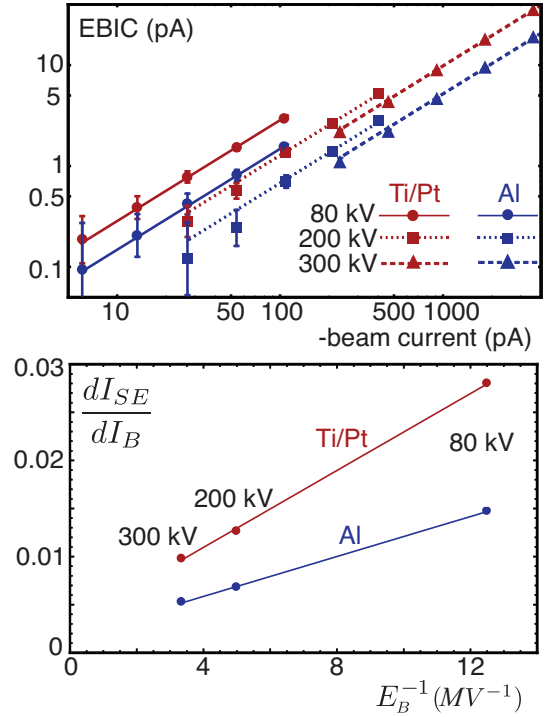

Figure 3. **EBIC vs beam current and SE yield vs inverse beam energy.** (*top*) The EBIC current from 5/25 nm Ti/Pt and 100 nm Al electrodes is shown (with fits to $I_{SE} = \delta \times I_B$) for five different beam currents I_B at each accelerating voltage of 80, 200, and 300 kV. The EBIC uncertainty is taken to be 0.1 pA. (*bottom*) The SE yield δ for each material, determined from the six fits above, is linear in E_B^{-1}, as predicted by Eq. 2.

A hole cannot fly through vacuum to be counted in an off-sample detector. Only the SE is detected — the fate of the corresponding hole, which remains in the sample, is unknown. SEEBIC imaging, on the other hand, detects the hole, and is sensitive to the sample properties not just at, but around the SE ejection point. Thus it can precisely locate the boundary of the conductance "watershed", even without the second SEEBIC image (i.e. double EBIC is not necessary — a single image with one TIA is sufficient). In the Fig. 2 device, the lithography is nearly perfect, but in other cases [21] SEEBIC imaging reveals a non-trivial boundary that is not along the axis of symmetry.

For bare electrode devices the EBIC signal responds to changes in the primary beam current and accelerating voltage as expected for SE emission (see Eq. 2). For 5/25 nm Ti/Pt and 100 nm Al electrodes, the SEEBICs are linear in the incident beam current (as measured with a Faraday cup [21]) at 80, 200, and 300 kV (Fig. 3, top). The slopes of these lines give the SE yield, i.e. the number of SE per primary electron, and are in the range 0.5–3%. The SE yield for each electrode material is inversely proportional to primary beam energy (Fig. 3, bottom), in agreement with Eq. 2. With only three data points
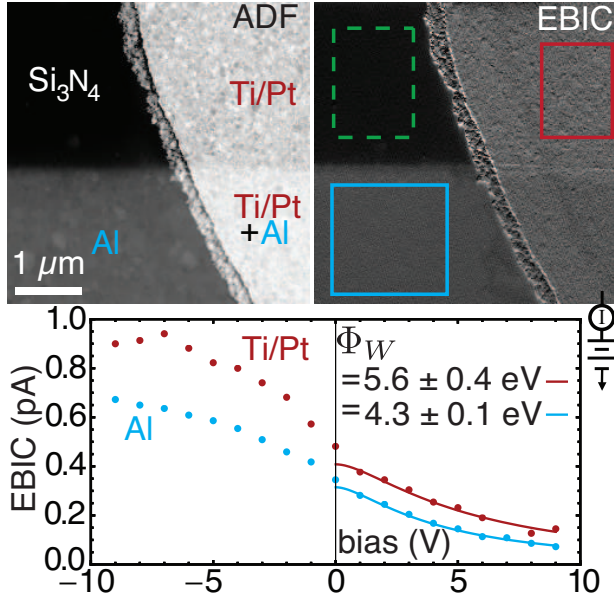
Figure 4. **ADF and EBIC images of Ti/Pt and Al electrodes and average SEEBIC from each material vs electrode bias.** The images show four different material combinations: the bare Si_3N_4 membrane, 5/25 nm Ti/Pt, 100 nm Al, and 5/25/100 nm Ti/Pt/Al. The plot shows the average signal in the SEEBIC image measured on the Al (blue box) and the Ti/Pt (red box), with the average current measured on the Si_3N_4 (green box) subtracted, for each bias value. The solid lines are fits to the SE emission current equation (Eq. 2) for $V > 0$, with the work functions and zero-bias currents as free parameters.
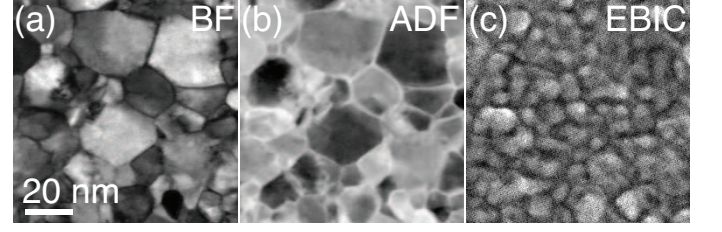
Figure 5. **Conventional STEM and STEM SEEBIC images of metallic grains in a Ti/Pt film.** Simultaneously acquired BF (a), ADF (b), and EBIC (c) images of a Ti/Pt (5/25 nm) electrode on a Si_3N_4 membrane.

for each of the two electrode materials, neither of which is freely suspended, we do not attempt to more precisely determine the power law exponent.

We have described edge contrast, contrast reversal between EBIC electrodes, material-dependent yields, $I_{SE} \propto I_B$, and $I_{SE} \propto E_B^{-1}$. Varying the EBIC electrode potential relative to ground (Fig. 4) further identifies SE as the source of these signals, and also indicates that SEEBIC imaging might be used to map material work functions. Biasing the TIA's input relative to ground, we see that positive (negative) bias decreases (increases) the EBIC signal, demonstrating active SE voltage contrast without an off-sample detector [19]. Similar analysis of the conventional STEM signals shows no bias dependence.

For positive electrode bias voltages, the measured EBIC scales according to the dependence given in Eq. 2, and indicates that about 60% of the SE have $E_{SE} < 9\,eV$. Fitting the data (Fig. 4) yields agreement with previously measured values for the work functions of Al and Pt [29]. Interestingly, we find that subsequent EBIC images of the same region give work function fit values that are systematically larger. For negative electrode bias voltages, we find that the SE yield increases as the bias magnitude increases. Both the increasing work functions

and the increasing (as opposed to constant) yields with negative bias can be attributed to surface contamination [30]. Even at monolayer thicknesses, SE emission is extremely sensitive to the presence of surface contaminants [31]. Imaging a sample in a merely high-vacuum (10^{-3}– 10^{-6} Pa) environment, such as exists in our TEM, is likely to alter the surface contamination layer. With an ultra-high-vacuum sample environment, however, work function could be mapped quantitatively at high resolution using STEM SEEBIC.

For a variety of materials the SEEBIC signal is thickness-independent, at least for samples $\lesssim 100$ nm thick, as expected for a surface-sensitive contrast mechanism [21]. Surprisingly, however, SEEBIC images can also show contrast based on buried surface texture. For instance, conventional STEM imaging of a 5/25 nm Ti/Pt electrode shows grains with characteristic lateral dimensions of about 25 nm (Fig. 5 a,b). For a thin film we expect grains with lateral dimensions comparable to the film thickness [32], and we expect platinum (atomic number $Z = 78$) to dominate STEM contrast relative to titanium ($Z = 22$). Clearly conventional STEM is imaging the thicker, heavier Pt layer in this bimetallic film. While some of the grain structure from Figs. 5 (a) and (b) is evident in the STEM EBIC image (c), the STEM EBIC image is dominated by grain structure with a length scale of about 5 nm, i.e. the thickness of the titanium film. This equivalence indicates that Fig. 5(c) is an image of the buried 5 nm Ti layer. Unlike in SEM SE imaging, STEM SEEBIC detects SE emitted from the bottom (beam exit) as well as the top (beam incident) surface of the sample. The SE yield of Pt is among the highest of the elements, and higher than that of Ti [27], so dominant Ti contrast in Fig. 5(c) suggests strong SE emission from the beam exit surface [33, 34]. Alternatively, the strength of the Ti signal relative to that of the Pt might be due to the generation of SE by inner-shell excitation events [35], since for these Ti has a substantially larger cross section than Pt [36].

V. CONCLUSION

In conclusion, we have demonstrated STEM SEEBIC imaging, which maps electronic properties such as connectivity and work function. Relative to standard EBIC, SEEBIC imaging gives contrast even in electric-field-free regions of a sample. Relative to STEM with off-sample SE detectors, STEM SEEBIC can provide a SE detection efficiency of unity, allowing direct measurement of net SE yield. Perhaps the most important distinction between STEM SEEBIC and these related techniques, however, is the differential contrast illustrated in each of the 'double EBIC' images of Fig. 2. Detecting the SE and the associated holes with an integral part of the device itself enables precision mapping of, for instance, the conductance watershed as shown. In nanoelectronic devices such as resistive random access memory (RRAM), knowledge of the connectivity landscape is key to understanding device function [37]. This application will be explored in future work.

ACKNOWLEDGMENTS

[1] F. J. Garcia de Abajo, "Optical excitations in electron microscopy," Reviews of Modern Physics **82**, 209 (2010).

[2] M. Mecklenburg, W. A. Hubbard, E. R. White, R. Dhall, S. B. Cronin, S. Aloni, and B. C. Regan, "Nanoscale temperature mapping in operating microelectronic devices," Science **347**, 629 (2015).

[3] T. E. Everhart, O. C. Wells, and R. K. Matta, "A novel method of semiconductor device measurements," Proceedings of the IEEE **52**, 1642 (1964).

[4] H. J. Leamy, "Charge collection scanning electron microscopy," Journal of Applied Physics **53**, R51 (1982).

[5] K. V. Ravi, C. J. Varker, and C. E. Volk, "Electrically active stacking faults in silicon," Journal of The Electrochemical Society **120**, 533 (1973).

[6] J. I. Hanoka and and R. O. Bell, "Electron-Beam-Induced Currents in Semiconductors," Annual Review of Materials Science **11**, 353 (1981).

[7] L. Pasemann, H. Blumtritt, and R. Gleichmann, "Interpretation of the EBIC contrast of dislocations in silicon," physica status solidi (a) **70**, 197 (1982).

[8] C. V. Hari Rao, H. E. Bates, and K. V. Ravi, "Electrical effects of SiC inclusions in EFG silicon ribbon solar cells," Journal of Applied Physics **47**, 2614 (1976).

[9] J. C. Manifacier and L. Szepessy, "Efficient sprayed In_2O_3:Sn ntype silicon heterojunction solar cell," Applied Physics Letters **31**, 459 (1977).

[10] K. Yamaguchi, N. Nakayama, H. Matsumoto, and S. Ikegami, "CdSCdTe solar cell prepared by vapor phase epitaxy," Japanese Journal of Applied Physics **16**, 1203 (1977).

[11] J. D. Poplawsky, C. Li, N. R. Paudel, W. Guo, Y. Yan, and S. J. Pennycook, "Nanoscale doping profiles within CdTe grain boundaries and at the CdS/CdTe interface revealed by atom probe tomography and STEM EBIC," Solar Energy Materials and Solar Cells **150**, 95 (2016).

[12] P. H. Rekemeyer, C. M. Chuang, M. G. Bawendi, and S. Gradecak, "Minority carrier transport in lead sulfide quantum dot photovoltaics," Nano Letters **17**, 6221 (2017).

[13] D. S. H. Chan, V. K. S. Ong, and J. C. H. Phang, "A direct method for the extraction of diffusion length and surface recombination velocity from an EBIC line scan: planar junction configuration," IEEE Transactions on Electron Devices **42**, 963 (1995).

[14] W. Shockley, "Problems related to p-n junctions in silicon," Solid-State Electronics **2**, 35 (1961).

[15] L. Reimer, *Scanning electron microscopy: physics of image formation and microanalysis*, 2nd ed. (Springer, Berlin, 1998).

[16] V. E. Cosslett, D. Fathy, T. G. Sparrow, and U. Valdre, "Investigation of Semiconductor Materials and Devices by High Voltage STEM Techniques," Kristall und Technik **14**, 1177 (1979).

[17] K. L. Bunker, J. C. Gonzalez, D. Batchelor, T. J. Stark, and P. E. Russell, "Development of a High Lateral Resolution Electron Beam Induced Current Technique for Electrical Characterization of InGaN-Based Quantum Well Light Emitting Diodes," MRS Online Proceedings Library Archive **743**, L10.10.1 (2002).

[18] E. R. White, A. Kerelsky, W. A. Hubbard, R. Dhall, S. B. Cronin, M. Mecklenburg, and B. C. Regan, "Imaging interfacial electrical transport in graphene-MoS$_2$ heterostructures with electron-beam-induced-currents," Applied Physics Letters **107**, 223104 (2015).

[19] M.-G. Han, J. A. Garlow, M. S.J. Marshall, A. L. Tiano, S. S. Wong, S.-W. Cheong, F. J. Walker, C. H. Ahn, and Y. Zhu, "Electron-beam-induced-current and active secondary-electron voltage-contrast with aberration-corrected electron probes," Ultramicroscopy **176**, 80 (2017).

[20] R. F. Egerton, P. Li, and M. Malac, "Radiation damage in the TEM and SEM," Micron International Wuhan Symposium on Advanced Electron Microscopy, **35**, 399 (2004).

[21] See supplementary material at [url to be inserted by publisher] for supplementary figures.

[22] L. Reimer and H. Kohl, *Transmission electron microscopy: physics of image formation*, 5th ed., Springer series in optical sciences No. 36 (Springer, New York, NY, 2008).

[23] H. Inada, D. Su, R. F. Egerton, M. Konno, L. Wu, J. Ciston, J. Wall, and Y. Zhu, "Atomic imaging using sec-

ondary electrons in a scanning transmission electron microscope: Experimental observations and possible mechanisms," Ultramicroscopy **111**, 865 (2011).

[24] M. S. Chung and T. E. Everhart, "Simple calculation of energy distribution of low-energy secondary electrons emitted from metals under electron bombardment," Journal of Applied Physics **45**, 707 (1974).

[25] J. D. Jackson, *Classical Electrodynamics*, 3rd ed. (Wiley, New York, 1999).

[26] J. G. Trump and R. J. Van de Graaff, "The Secondary Emission of Electrons by High Energy Electrons," Physical Review **75**, 44 (1949).

[27] H. Seiler, "Secondary electron emission in the scanning electron microscope," Journal of Applied Physics **54**, R1 (1983).

[28] J. Cazaux, "Some considerations on the secondary electron emission, δ, from $e-$ irradiated insulators," Journal of Applied Physics **85**, 1137 (1998).

[29] J. Hölzl, ed., *Solid surface physics*, Springer tracts in modern physics No. 85 (Springer, Berlin, 1979).

[30] R. Davies, *Measurement of Angle-Resolved Secondary Electron Spectra*, Ph.D. thesis, Utah State University, Logan, UT (1999).

[31] W. Chang, J. Dennison, J. Kite, and R. Davies, "Effects of evolving surface contamination on spacecraft charging," American Institute of Aeronautics and Astronautics (38th Aerospace Sciences Meeting and Exhibit, 2000).

[32] C. V. Thompson, "Grain Growth in Thin Films," Annual Review of Materials Science **20**, 245 (1990).

[33] V. N. E. Robinson, "The dependence of emitted secondary electrons upon the direction of travel of the exciting electron," Journal of Physics D: Applied Physics **8**, L74 (1975).

[34] L. Reimer and H. Drescher, "Secondary electron emission of 10-100 keV electrons from transparent films of al and au," Journal of Physics D: Applied Physics **10**, 805 (1977).

[35] Howie A., "Recent developments in secondary electron imaging," Journal of Microscopy **180**, 192 (1995).

[36] R. D. Leapman, P. Rez, and D. F. Mayers, "K, L, and M shell generalized oscillator strengths and ionization cross sections for fast electron collisions," The Journal of Chemical Physics **72**, 1232 (1980).

[37] W. A. Hubbard, A. Kerelsky, G. Jasmin, E. R. White, J. Lodico, M. Mecklenburg, and B. C. Regan, "Nanofilament Formation and Regeneration During Cu/Al_2O_3 Resistive Memory Switching," Nano Letters **15**, 3983 (2015).